SPEAR-Net: Self-Prior Enhanced Artifact Removal Network for Limited-Angle DECT

Kai Chen, Chunfeng Yang, Hui Tang, Xu Ji, Gouenou Coatrieux, Jean-Louis Coatrieux, Yang Chen

▶ **To cite this version:**

Kai Chen, Chunfeng Yang, Hui Tang, Xu Ji, Gouenou Coatrieux, et al.. SPEAR-Net: Self-Prior Enhanced Artifact Removal Network for Limited-Angle DECT. IEEE Transactions on Instrumentation and Measurement, 2023, 72, pp.4003614. 10.1109/TIM.2023.3260280 . hal-04090022

HAL Id: hal-04090022
https://hal.science/hal-04090022

Submitted on 16 May 2023

HAL is a multi-disciplinary open access archive for the deposit and dissemination of scientific research documents, whether they are published or not. The documents may come from teaching and research institutions in France or abroad, or from public or private research centers.

L'archive ouverte pluridisciplinaire **HAL**, est destinée au dépôt et à la diffusion de documents scientifiques de niveau recherche, publiés ou non, émanant des établissements d'enseignement et de recherche français ou étrangers, des laboratoires publics ou privés.

Distributed under a Creative Commons Attribution - NonCommercial 4.0 International License

This article has been accepted for publication in IEEE Transactions on Instrumentation and Measurement. This is the author's version which has not been fully edited and content may change prior to final publication. Citation information: DOI 10.1109/TIM.2023.3260280

SPEAR-Net: Self-Prior Enhanced Artifact Removal Network for Limited-Angle DECT

Kai Chen, Chunfeng Yang, Hui Tang , Xu Ji, Gouenou Coatrieux, *Senior Member, IEEE*, Jean-Louis Coatrieux *Life fellow, IEEE*, and Yang Chen, *Senior Member, IEEE*

***Abstract*—Dual-energy computed tomography (DECT) is a fully functional instrument for disease detection in clinical practice because of its ability to identify substances and quantify materials. In some practical applications, due to the limitation of scanning conditions, projection data can only be collected from a limited angle, and the consistency of measurement cannot be guaranteed. Existing dual-energy CT reconstruction methods fail to address well the severe artifacts and noise in dual-energy CT images caused by limited-angle scanning. In this paper, we proposed a Self-Prior Enhanced Artifact Removal Network (SPEAR-Net) for limited-angle DECT, which can effectively combine the complementary information in the high- and low-energy domains and self-prior information to contribute positively to the reconstruction of high-quality dual-energy CT images. The SPEAR-Net consists of an image-domain self-prior network(IP-Net), two dual-energy image-domain networks(DIP-Net), and a dual-energy sinogram-domain self-prior network(DSP-Net). Specifically, the IP-Net and DIP-Net are adopted to extract the features of the dual-energy CT reconstructed images under dual-quarter scanning as prior information. The self-prior projection obtained from the forward projection of the prior CT image is harnessed by DSP-Net to complete the dual-energy limited-angle projection data and to facilitate the performance of SPEAR-Net in removing artifacts in the reconstructed dual-energy images. Qualitative and quantitative analyses demonstrate the superior capability of SPEAR-Net in dual-energy limited-angle projection data complementation, detail preservation, and artifact removal. Two popular DECT applications, virtual non-contrast (VNC) imaging and iodine contrast agent quantification, reveal that images reconstructed by SPEAR-Net have promising clinical significance.**

***Index Terms*—Dual-energy computed tomography, limited-angle reconstruction, virtual non-contrast imaging, iodine contrast agent quantification, deep learning.**

This work was supported by the National Key Research and Development Program of China (2022YFE0116700), in part by the National Key Research and Development Program of China (2022YFC2401600), in part by the Key Research and Development Programs in Jiangsu Province of China (BE2021703 and BE2022768), and part by Jiangsu Province Science Foundation for Youths (BK20220825). Corresponding author: Hui Tang (e-mail: corinna@seu.edu.cn) and Xu Ji (e-mail: xuji@seu.edu.cn.)

Kai Chen is with the School of Cyber Science and Engineering, Southeast University, Nanjing 210096, and also with the Key Laboratory of Computer Network and Information Integration (Ministry of Education), Southeast University, Nanjing 210096, China.

Chunfeng Yang, Hui Tang, and Xu Ji are with the School of Computer Science and Engineering, Southeast University, Nanjing 210096.

G. Coatrieux is with the IMT Atlantique, Inserm, LaTIM UMR1101,Brest 29000, France.

J.-L. Coatrieux is with the Laboratoire Traitement du Signal et de l'Image, Universit ´e de Rennes 1, F-35000 Rennes, France, with the Centre de Recherche en Information Biom´edicale Sino-francais,35042 Rennes, France, and also with the National Institute for Health and Medical Research, F-35000 Rennes, France.

Yang Chen is with the Jiangsu Provincial Joint International Research Laboratory of Medical Information Processing, School of Computer Science and Engineering, Southeast University, Nanjing, 210096, China, Jiangsu Key Laboratory of Molecular and Functional Imaging, Department of Radiology, Zhongda Hospital, Southeast University, Nanjing 210009, China, and also with the School of Cyber Science and Engineering, Southeast University, Nanjing 210096, China, and also with the Key Laboratory of Computer Network and Information Integration Southeast University), Ministry of Education, Nanjing 210096, China.

I. Introduction

X-ray computed tomography (CT) is one of the measurement instruments widely used in medical diagnosis, industrial testing, and security inspection because of its fast imaging speed and high imaging quality [1]–[5]. Dual-energy computed tomography (DECT) is becoming increasingly popular because of its outstanding performance in material identification, lesion detection, and tissue characterization [6]–[10]. However, due to the limitations of scanning conditions [11]–[14], dual-energy projection data can only be acquired within a limited range of angles. In these dual-energy CT practices, incomplete scan angles result in severe artifacts in the reconstructed images, which significantly reduces the diagnostic accuracy of the clinician. To solve this problem, a large number of algorithms have been developed to cope with limited-angle CT reconstruction. These algorithms can be divided into three categories: reconstruction by compensating for missing data in the projection domain, reconstruction with prior information in the image domain, and reconstruction with deep learning-based methods.

Completing the missing data in the projection domain is an effective method to improve the quality of dual-energy limited-angle reconstructed images. In 2008, Duan et al. introduced the TV minimization model into the projection domain for the metal artifact correction problem and repaired the missing data according to the sparsity of the projection domain to compensate for the projection domain image information better [15]. In 2012, Li et al. proposed a new method for repairing sinograms by combining sinogram-like decomposition with eigenvector-guided interpolation, in which each missing sinogram point lies in a set of sinogram-like curves and is estimated by eigenvector-guided interpolation to maintain the continuity of the sinogram texture [16]. In 2014, Kalke et al. consider the curvature feature of the sinogram as an approximate sinusoidal wave in a limited region and perform compensatory restoration of the projected sinogram by solving the curvature feature, and the method obtains better results in suppressing artifacts and reducing structural blur [17]. Even though the above projection compensation methods obtain promising reconstruction results by exploiting

This article has been accepted for publication in IEEE Transactions on Instrumentation and Measurement. This is the author's version which has not been fully edited and content may change prior to final publication. Citation information: DOI 10.1109/TIM.2023.3260280

the characteristics of the projection domain data in many aspects, in the limited-angle application, the projection compensation is not effective for the limited-angle reconstruction because the continuous projection data is severely damaged. In 2015, Martin et al. addressed the limited-angle projection problem by describing the sparsity of the projection domain using the Total Generalized Variation (TGV) model to achieve compensation for missing projection data [18]. In 2016, Choi et al. proposed a truncated projection compensation method based on a wavelet-tight framework based on the sparsity of the projection domain images, which was applied in limited-angle reconstruction [19]. By exploiting and utilizing the prior knowledge of projection domain data for limited-angle CT reconstruction, it is conducive to improving the quality of reconstructed images under projection data missing conditions.

To improve the quality of CT reconstruction images, the methods based on prior information in the image domain have been investigated for limited-angle CT imaging. In 2008, Chen et al. proposed a Prior Image Constrained Compressed Sensing (PICCS) reconstruction algorithm, which uses the projections obtained from the dynamic projection dataset to reconstruct the prior image, and combines the prior image as a constraint with the CS to reconstruct each frame in the dynamic CT image sequence [20]. In 2012, Lu et al. proposed a strategy of forming a double dictionary using image blocks of two different quality prior images, high and low, to enhance the quality of incomplete angle reconstruction images [21]. In 2013, Schorr et al. applied contours as reconstruction region constraints to a limited-angle reconstruction of flat objects to suppress finite angle artifacts [22]. Wu et al. proposed a Feature Constrained Compressed Sensing (FCCS) reconstruction model based on PICCS, which used the atlas of a prior image feature decomposition as a constraint term to obtain high-quality reconstructed images in limited-angle reconstruction [23]. In 2014, Zhang et al. proposed a Deformed Prior Image-based Reconstruction (DPIR) reconstruction algorithm based on the PICCS algorithm, which further reduced the requirements for prior images, and obtained better results in the limited-angle reconstruction [24]. In 2015, Dang et al. studied in depth the problem of balancing the prior image constraint term with the fidelity term in the reconstruction process to improve the robustness of the prior image-based reconstruction method [25]. The limited-angle CT reconstruction method based on the prior information in the image domain can assist in suppressing the blurring artifacts caused by the missing limited-angle projections and improving the quality of the reconstructed images. However, the limitation of this method is that it overly relies on the prior information of the object to be reconstructed, and in some practical CT applications, it is quite difficult to obtain structurally similar prior images or high-precision contour information in advance, thus limiting the application of this type of algorithm.

Recently, DL-based algorithms have attracted great attention in the field of medical imaging [26]–[33]. In 2013, Pelt et al. proposed a reconstruction method that uses the autonomous learning capability of a Convolutional Neural Network (CNN) to acquire prior information, and also demonstrated that the method can be regarded as an equivalent combination of filtering and inverse projection operations. Experimental results show that the method can quickly reconstruct CT images with good results using the projection information acquired from the detector [34]. In 2016, Yang et al. defined a new network architecture ADMM-Net (Alternative Direction Method of Multipliers-Net) on the data flow graph. In this network, it is the step-by-step solution of the CS-based nuclear magnetic resonance (MRI) model using the ADMM method that is used to derive this data flow graph. The final results demonstrate that this algorithm can obtain high-quality reconstructed images in MRI reconstruction models quickly [35]. In 2017, Jin et al. proposed a depth reconstruction algorithm consisting of a combination of an analytic algorithm and a convolutional neural network. In this reconstruction algorithm, the physical output of the imaging system is first achieved using the FBP algorithm, but the output image obtained will have a large number of artifacts. The CNN network is then used to combine multi-resolution decomposition with residual learning to achieve the effect of preserving the image structure and reducing the artifacts. The final results point out that the algorithm obtains higher quality reconstructed images in terms of parallel beam sparse projection reconstruction [36]. The CD-Net (Comprehensive Domain Network) proposed by Zhang et al. exploited information redundancy with spectral complementarity to improve image quality and reduce radiation dose for DECT imaging [37]. Zhang et al. developed the Comprehensive Learning Enabled Adversarial Reconstruction (CLEAR) method for Low-Dose CT Imaging [38]. Hu et al.proposed a novel reconstruction framework termed Deep Iterative Optimization-based Residual-learning (DIOR) for limited-angle CT [39]. Quantitative and qualitative results show that the DIOR brings a promising improvement in artifact removal, detail restoration, and edge preservation. Hu et al. developed a method termed Single-shot ProjectionError Correction Integrated Adversarial Learning (SPECIAL) progressive-improvement strategy, which could effectively combine the complementary information contained in the image domain and projection domain, and greatly improve the reconstructions at the expense of small computational cost [40]. Previous works neglected feature fusion and data complementation for dual-energy limited-angle CT reconstruction using self-prior knowledge in the projection and image domains. In this paper, we make the following contributions:

- The prior information of a dual-energy CT image under alternating high- and low-energy dual quarter-scan (half-scan) was extracted, which made a great contribution to guiding SPEAR-Net in feature learning, artifact removal, and detail protection.
- Projections under full-scan are masked with the prior information of the dual-energy CT. This masking operation corrects the noise caused by the limited-angle scan and amplifies the statistical distribution of the true projection data under full-scan.
- Two CT images under high and low energy quarter-scan are fused with the masked features for feature-rich, which facilitates the enhancement of the global features of the

This article has been accepted for publication in IEEE Transactions on Instrumentation and Measurement. This is the author's version which has not been fully edited and content may change prior to final publication. Citation information: DOI 10.1109/TIM.2023.3260280

projection and the data complementation of the dual-energy limited-angle.

- Two deep learning networks that adopt a novel multi-level consistency loss are developed that exploit simultaneously redundant information in the high-and low-energy domains and rich prior information in the projection and image domains for dual-energy limited-angle CT reconstruction.

The rest of this paper is organized as follows. Section II gives the mathematical model of SPEAR-Net and the details of the neural network architecture. The result and analysis are presented in the section III. Section IV will discuss relevant issues and present conclusions.

II. Methodology

A. One-Step DECT Limited-angle Reconstruction Strategy

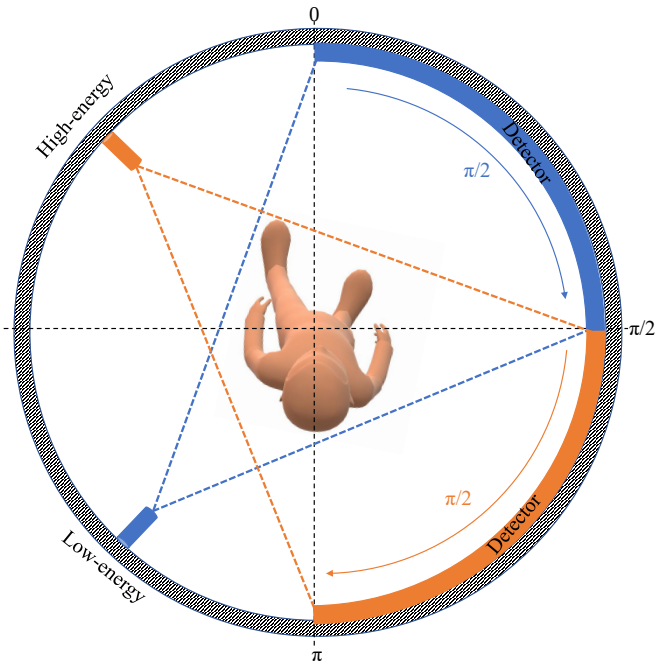

Fig. 1. High- and low-energy complementary dual-quarter limited-angle CT scanning scheme.

The energy redundancy of DECT and self-prior information are utilized to develop a dual-energy CT limited-angle data acquisition strategy as shown in Fig.1. High- and low-energy x-source crossed 90° scan, and the patient's anatomical information is scanned in the range of $0° \sim 90°$ and $90° \sim 180°$ by alternating low- and high- energy. In this way, the patient is half-scanned by dual-energy CT. It also provides as much patient information as possible and minimizes scan times and radiation doses. The self-prior enhanced artifact removal network (SPEAR-Net) for one-step dual-energy limited-angle reconstruction is shown in Fig.2(A). The SPEAR-Net consists of an image-domain self-prior network(IP-Net), a dual-energy sinogram-domain self-prior network(DSP-Net), and two dual-energy image-domain self-prior networks(DIP-Net). Specifically, the image domain self-prior information is provided by IP-Net for guiding SPEAR-Net in feature learning, artifact removal, and detail protection. The sinogram domain self-prior information is employed by DSP-Net to better complete the projection domain data for dual-energy limited-angle reconstruction. DIP-Net simultaneously reduces noise and removes artifacts in the high- and low-energy domains for limited-angle CT images. The procedure of extracting self-prior information $\begin{bmatrix} \widehat{\mathbf{I}_l^L} \\ \widehat{\mathbf{I}_l^H} \end{bmatrix}$ from dual-energy limited-angle CT image $\begin{bmatrix} \mathbf{I}_l^L \\ \mathbf{I}_l^H \end{bmatrix}$ can be achieved by the function f_{IP}:

$$\begin{bmatrix} \widehat{\mathbf{I}_l^L} \\ \widehat{\mathbf{I}_l^H} \end{bmatrix} = f_{\text{IP}}^* \begin{bmatrix} \mathbf{I}_l^L \\ \mathbf{I}_l^H \end{bmatrix} \tag{1}$$

$$f_{\text{IP}}^* = \underset{f_{\text{IP}}}{\operatorname{argmin}} \left\| f_{\text{IP}} \begin{bmatrix} \mathbf{I}_l^L \\ \mathbf{I}_l^H \end{bmatrix} - \begin{bmatrix} \mathbf{I}_a^L \\ \mathbf{I}_a^H \end{bmatrix} \right\|, \tag{2}$$

where $\widehat{\mathbf{I}_l^i}$ and $\mathbf{I}_a^i$ with $i = (L, H)$ represent the DE limited-angle self-prior CT images and the DE CT images with reconstructed artifacts from incomplete dual-energy projection data. A Radon transform operator embedded in the Tensorflow framework is employed to obtain DE limited-angle self-prior projection data.

$$\begin{bmatrix} \widehat{\mathbf{p}_l^L} \\ \widehat{\mathbf{p}_l^H} \end{bmatrix} = \mathcal{R} \begin{bmatrix} \widehat{\mathbf{I}_l^L} \\ \widehat{\mathbf{I}_l^H} \end{bmatrix} \tag{3}$$

where $\begin{bmatrix} \widehat{\mathbf{p}_l^L} \\ \widehat{\mathbf{p}_l^H} \end{bmatrix}$ denote the projections corresponding to $\begin{bmatrix} \widehat{\mathbf{I}_l^L} \\ \widehat{\mathbf{I}_l^H} \end{bmatrix}$.

The dual-energy limited-angle prior projection is masked as follows:

$$\begin{aligned} \widehat{\mathbf{p}_m^L} &= \widehat{\mathbf{p}_l^L} * (1 - \mathbf{M}_L) + \mathbf{p}_f^L * \mathbf{M}_L \\ \widehat{\mathbf{p}_m^H} &= \widehat{\mathbf{p}_l^H} * (1 - \mathbf{M}_H) + \mathbf{p}_f^H * \mathbf{M}_H \end{aligned} \tag{4}$$

Where $\mathbf{M}_L = \begin{bmatrix} \mathbf{M}_L^1 \\ \mathbf{M}_L^2 \\ \mathbf{M}_L^3 \\ \mathbf{M}_L^4 \end{bmatrix}_{576\times763}$, $\mathbf{M}_L^1 = \begin{bmatrix} 1 & \cdots & 1 \\ \vdots & \ddots & \vdots \\ 1 & \cdots & 1 \end{bmatrix}_{144\times736}$, $\mathbf{M}_L^2 = \mathbf{M}_L^3 = \mathbf{M}_H^4 = \begin{bmatrix} 0 & \cdots & 0 \\ \vdots & \ddots & \vdots \\ 0 & \cdots & 0 \end{bmatrix}_{144\times736}$, $\mathbf{M}_H = \begin{bmatrix} \mathbf{M}_H^1 \\ \mathbf{M}_H^2 \\ \mathbf{M}_H^3 \\ \mathbf{M}_H^4 \end{bmatrix}_{576\times763}$, $\mathbf{M}_H^2 = \begin{bmatrix} 1 & \cdots & 1 \\ \vdots & \ddots & \vdots \\ 1 & \cdots & 1 \end{bmatrix}_{144\times736}$, $\mathbf{M}_H^1 = \mathbf{M}_H^3 = \mathbf{M}_H^4 = \begin{bmatrix} 0 & \cdots & 0 \\ \vdots & \ddots & \vdots \\ 0 & \cdots & 0 \end{bmatrix}_{144\times736}$, and $\mathbf{p}_f^i$ with $i = (L, H)$ represent the DE projection under full-scan.

This article has been accepted for publication in IEEE Transactions on Instrumentation and Measurement. This is the author's version which has not been fully edited and content may change prior to final publication. Citation information: DOI 10.1109/TIM.2023.3260280

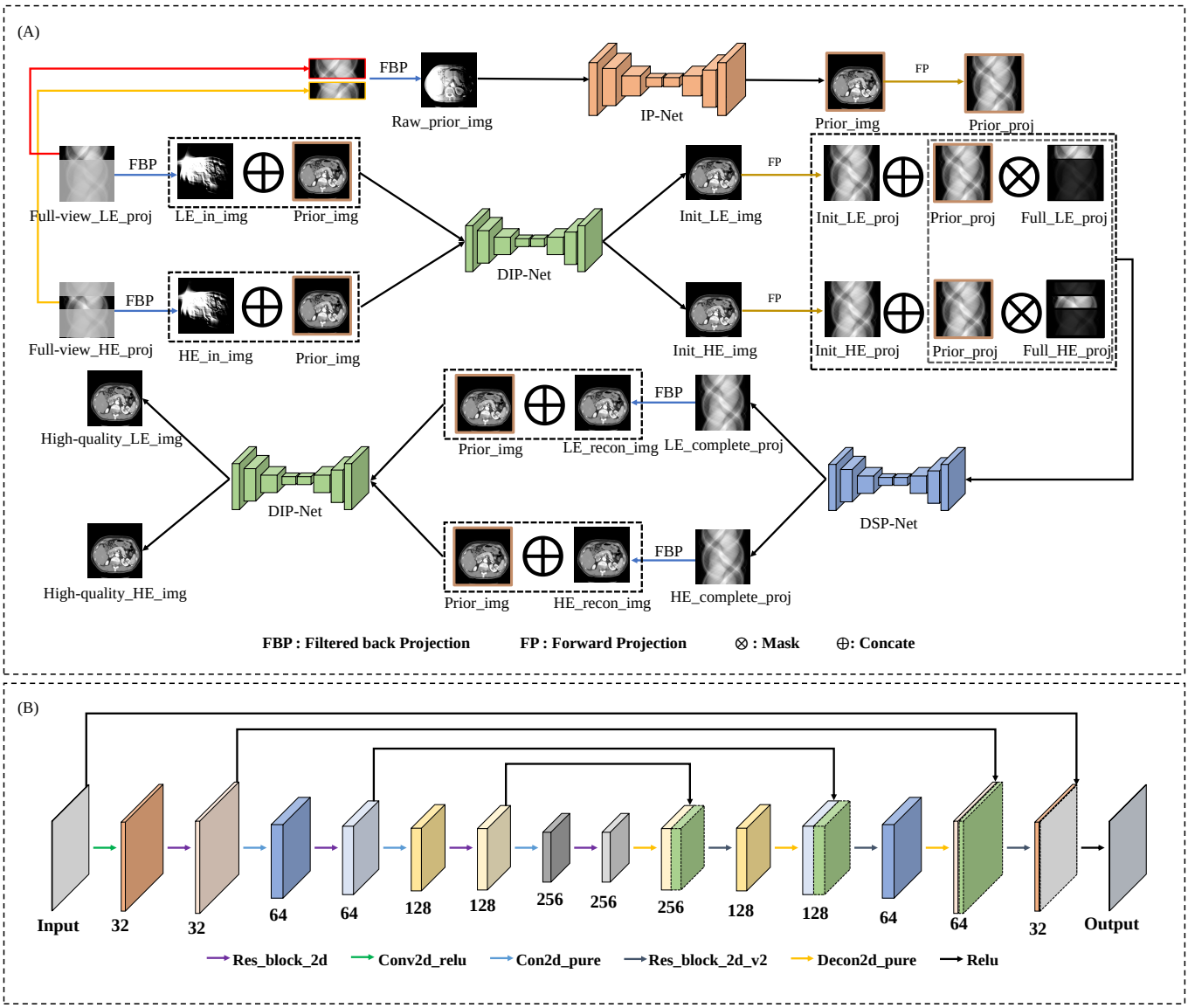

Fig. 2. The one-step DECT limited-angle reconstruction strategy based on SPEAR-Net. (A)The SPEAR-Net consists of an image-domain self-prior network(IP-Net), a dual-energy sinogram-domain self-prior network(DSP-Net), and two dual-energy image-domain self-prior networks(DIP-Net). (B)The same Encoder-Decoder architecture of IP-Net, DIP-Net, and DSP-Net.

The masked projection is simultaneously complemented and restored using a function f_{DSP} in the high and low energy domains.

$$\begin{bmatrix} \widetilde{\mathbf{p}_f^L} \\ \widetilde{\mathbf{p}_f^H} \end{bmatrix} = \begin{bmatrix} \widehat{\mathbf{p}_m^L} \\ \widehat{\mathbf{p}_m^H} \end{bmatrix} - f_{\mathrm{DSP}}^* \begin{bmatrix} \widehat{\mathbf{p}_m^L} \\ \widehat{\mathbf{p}_m^L} \end{bmatrix}, \tag{5}$$

$$f_{\mathrm{DSP}}^* = \underset{f_{\mathrm{DSP}}}{\operatorname{argmin}} \left\| f_{\mathrm{DSP}} \begin{bmatrix} \widetilde{\mathbf{p}_m^L} \\ \widetilde{\mathbf{p}_m^H} \end{bmatrix} - \begin{bmatrix} \mathbf{p}_a^L \\ \mathbf{p}_a^H \end{bmatrix} \right\|, \tag{6}$$

where $\widetilde{\mathbf{p}_f^i}$ and $\widehat{\mathbf{p}_m^i}$ with $i = (L, H)$ represent the approximate solution to the full scan projection, the masked limited-angle projection, respectively. $\begin{bmatrix} \mathbf{p}_a^L \\ \mathbf{p}_a^H \end{bmatrix}$ represent projections corresponding to $\begin{bmatrix} \mathbf{I}_a^L \\ \mathbf{I}_a^H \end{bmatrix}$. The sinogram domain and image domain are bridged by a Radon transform operator embedded in the Tensorflow framework:

$$\begin{bmatrix} \widetilde{\mathbf{I}_f^L} \\ \widetilde{\mathbf{I}_f^H} \end{bmatrix} = \mathcal{R}^{-1} \begin{bmatrix} \widetilde{\mathbf{p}_f^L} \\ \widetilde{\mathbf{p}_f^H} \end{bmatrix}, \tag{7}$$

The image post-processing is adopted to further remove artifacts using a function f_{DIP}:

$$\begin{bmatrix} \mathbf{I}_c^{L,*} \\ \mathbf{I}_c^{H,*} \end{bmatrix} = \begin{bmatrix} \widetilde{\mathbf{I}_f^L} \\ \widetilde{\mathbf{I}_f^H} \end{bmatrix} - f_{\mathrm{DIP}}^* \begin{bmatrix} \widetilde{\mathbf{I}_f^L} \\ \widetilde{\mathbf{I}_f^H} \end{bmatrix}, \tag{8}$$

$$f_{\mathrm{DIP}}^* = \underset{f_{\mathrm{DIP}}}{\operatorname{argmin}} \left\| f_{\mathrm{DIP}} \begin{bmatrix} \widetilde{\mathbf{I}_c^L} \\ \widetilde{\mathbf{I}_c^H} \end{bmatrix} - \begin{bmatrix} \mathbf{I}_a^L \\ \mathbf{I}_a^H \end{bmatrix} \right\|, \tag{9}$$

This article has been accepted for publication in IEEE Transactions on Instrumentation and Measurement. This is the author's version which has not been fully edited and content may change prior to final publication. Citation information: DOI 10.1109/TIM.2023.3260280

where $\begin{bmatrix} \mathbf{I}_a^L \\ \mathbf{I}_a^H \end{bmatrix}$ and $\begin{bmatrix} \widetilde{\mathbf{I}_f^L} \\ \widetilde{\mathbf{I}_f^H} \end{bmatrix}$ and represent the corresponding images of $\begin{bmatrix} \mathbf{p}_a^L \\ \mathbf{p}_a^H \end{bmatrix}$ and $\begin{bmatrix} \widetilde{\mathbf{p}_f^L} \\ \widetilde{\mathbf{p}_f^H} \end{bmatrix}$, respectively. $\begin{bmatrix} \mathbf{I}_c^{L,*} \\ \mathbf{I}_c^{H,*} \end{bmatrix}$ is an optimal estimate of the clinical normal dose DE images.

B. Details of the IP-Net, DIP-Net, and DSP-Net

The IP-Net, DIP-Net, and DSP-Net share the same encoder-decoder architecture as shown in Fig.2(B). The encoder can effectively extract rich low-level features of low-dimensional manifolds and has good robustness to noise and disturbance. The decoder is also able to complement dual-energy limited-angle projection from the encoding space and restore high-quality reconstructed images. The skip connections deliver the encoder's low-level and high-resolution properties to higher-level and fine-grained properties through serial operations, avoiding loss of detail and speeding up the flow of information. Both DIP-Net and DSP-Net have to concate the input image and the prior image in the channel dimension during input, while IP-Net can just input the image directly. The number of feature channels increases from 32 to 256 and then decreases from 256 to 1, with the fusing of a 1×1 convolution layer. The kernel size of all convolution and deconvolution is 3×3, except for the last layer. The ResBlock encompasses two sequential convolutions and a residual connection. To avoid resolution loss, the convolution with a stride set to 2 is used for down-sampling and the deconvolution with the same stride is employed for up-sampling. Con2d_relu differs from Con2d_pure in whether the convolution is followed by activation with the ReLU function. The activation function of IP-Net is ReLU, and that of DIP-Net and DSP-Net is LeakyReLU.

The mean absolute error (MAE) and the structural similarity index (SSIM) were combined to design the loss function for SPEAR-Net [41]–[43]. MAE calculates the loss in Eq.(10):

$$\mathcal{L}^{\mathrm{MAE}}(\mathbf{y}, \mathbf{x}) = \frac{1}{m} \sum_{i=1}^{m} |\mathbf{y}_i - \mathbf{x}_i|, \tag{10}$$

where $\mathbf{x}$ denotes the reconstructed image, $\mathbf{y}$ denotes the corresponding reference image, and m is the number of pixels. The subscript i indicates the i^{th} pixel. The SSIM is defined as follows:

$$\mathrm{SSIM}(\boldsymbol{x}_1, \boldsymbol{x}_2) = \frac{(2\mu_{x_1}\mu_{x_2} + c_1)(2\sigma_{x_1,x_2} + c_2)}{(\mu_{x_1}^2 + \mu_{x_2}^2 + c_1)(\sigma_{x_1}^2 + \sigma_{x_2}^2 + c_2)}, \tag{11}$$

where μ denotes the mean value of the image, σ^2 is the variance of the image, and $\sigma_{(\boldsymbol{x}_1\boldsymbol{x}_2)}$ indicates the covariance of two images. c_1 and c_2 are constants associated with the value range of the image. The SSIM error is formulated as:

$$\mathcal{L}^{\mathrm{SSIM}}(\mathbf{y}, \mathbf{x}) = 1 - \mathrm{SSIM}(\mathbf{y}, \mathbf{x}), \tag{12}$$

Dual-energy CT is used for the quantitative analysis of substances based on the difference in attenuation changes of different substances at high and low energies. We developed the dual-energy MAE to utilize this characteristic:

$$\mathcal{L}^{\mathrm{Diff}}(\mathbf{y}, \mathbf{x}) = \mathrm{MAE}(\mathbf{Diff}_{\mathbf{y}}, \mathbf{Diff}_{\mathbf{x}}), \tag{13}$$

The differences between low-energy data and high-energy data are defined as:

$$\mathbf{Diff} = \mathbf{D}_{\mathrm{L}} - \mathbf{D}_{\mathrm{H}}, \tag{14}$$

where $\mathbf{D}_{\mathrm{L}}$ and $\mathbf{D}_{\mathrm{H}}$ denote low-energy data and high-energy data. The multi-level consistency loss in SPEAR-Net is designed as follows:

$$\mathcal{L} = \alpha \cdot \mathcal{L}^{\mathrm{MAE}} + \beta \cdot \mathcal{L}^{\mathrm{SSIM}} + \gamma \cdot \mathcal{L}^{\mathrm{Diff}}, \tag{15}$$

C. DECT Clinical Applications

This study is dedicated to virtual imaging and iodine quantification, which are widely considered to be the two most common clinical applications of dual-energy CT. A VNC image is an image in which the contrast agent used is artificially removed. Modeling CT scans without contrast and potentially alleviating the clinical need for CT scans without contrast. This quantitative iodine map is employed for the subjective assessment of various lesions. The method is performed in [44] for material decomposition. Eq.(16) illustrates the dependence between the base material image and the energy-resolved DECT image $f(r)$.

$$\mathbf{b}(r) = \mathbf{W} \cdot f(r), \tag{16}$$

Where $\mathbf{W}$ is a matrix of weight coefficients, which has a size of 2×2. The water and iodine contrast agent ROIs in the DECT images were selected to correct the weighting factor matrix W. They are taken as b1 = 1 and b2 = 0, and b1 = 1 and b2 = 1. Eq.(17)and Eq.(18) were used by ROIs to calibrate the measurements.

$$b_1 = \mathbf{W} \cdot c_1, \text{ with } \mathrm{b}_1 = \begin{bmatrix} 1 \\ 0 \end{bmatrix} \text{ and } \mathrm{c}_1 = \begin{bmatrix} c_{1L} \\ c_{1H} \end{bmatrix}, \tag{17}$$

and,

$$b_2 = \mathbf{W} \cdot c_2, \text{ with } \mathrm{b}_2 = \begin{bmatrix} 1 \\ 1 \end{bmatrix} \text{ and } \mathrm{c}_1 = \begin{bmatrix} c_{2L} \\ c_{2H} \end{bmatrix}, \tag{18}$$

where the $c_{1\mathrm{L}}$ and $c_{1\mathrm{H}}$ are the measured CT number of high- and low-energy CT image water ROIs, respectively. $c_{2\mathrm{L}}$ and $c_{2\mathrm{H}}$ are the measured CT number of high- and low-energy CT image iodine ROIs, respectively. The weighting coefficient matrix W can be determined by Eq. (17) and Eq. (18), and the VNC image and iodogram of a specific material can be reconstructed using the DECT images obtained from full-scan and limited-angle scanning. We performed a quantitative comparison of material-specific images with the results obtained from DECT images using the full-scan approach as a baseline.

III. Experiment results and analysis

A. Experimental datasets

In this study, the data set contains clinical DECT images of 22 patients who had scanned under 100 kVp and 140 kVp with an iodine contrast-enhanced SOMATOM Definition Flash DECT scanner (Siemens Healthineers, Forchheim, Germany). All scans were performed at the PLA General Hospital in Nanjing, China, with institutional review board approval and patient consent forms and were adherent to the tenets of the Declaration of Helsinki. Data from 17 cases were used to train

This article has been accepted for publication in IEEE Transactions on Instrumentation and Measurement. This is the author's version which has not been fully edited and content may change prior to final publication. Citation information: DOI 10.1109/TIM.2023.3260280

all networks in the experiment, data from the 2 cases were used as a validation set, and the remaining 3 cases were treated as a test set. The projection data were simulated based on a simple Radon transform of clinical DECT images. The original spectra for the clinical DECT images are 100 kVp (low-energy) and 140 kVp (high-energy), respectively. Mean energies for the 100 kVp and 140 kVp spectra were approximately 65 keV and 80 keV, respectively. The Radon transform represents single-energy (with a mean energy of 100 kVp and 140 kVp spectra) forward projections. The source-to-detector distance and the source-to-rotation centers were 1085.6mm and 595.0mm. The 736 detection elements are available, each with a size of 1.2858 mm. All CT images are 0.80mm $\times$ 0.80 mm pixels in size. The projection data with the size of 576×736 and the images with the size of 512×512 were directly used to train SPEAR-Net. All forward projection and reconstruction methods in this paper are implemented by a MATLAB Toolbox (http://www.eecs.umich.edu/∼fessler/code/). A Poisson noise in Eq. (19) was added for forwarding projection.

$$Z_i \sim Poisson\{Z_{0i} \cdot exp(-P_i)\}, i = 1, 2, ..., N. \tag{19}$$

where Z_i is the number of transmitted photons, Z_{0i} is the incident X-ray photon intensity, P_i is the line integral of attenuation coefficients along the i^{th} ray path, and N is the total number of X-ray paths. CT values in Hounsfield Unit (HU) can be represented as the linear transformation of attenuation coefficient μ with the following equation:

$$HU = 1000 \times \frac{\mu - \mu_{water}}{\mu_{water}}, \tag{20}$$

The relationships between 576-view DE projections p_l and projections p_f under full-scan are brideged by the Eq(21):

$$\begin{aligned} \mathbf{p}_l^{\mathrm{L}}(A_1 : A_1 + Angle) &= \mathbf{p}_f^{\mathrm{L}}(A_1 : A_1 + Angle), \\ \mathbf{p}_l^{\mathrm{H}}(A_2 : A_2 + Angle) &= \mathbf{p}_f^{\mathrm{H}}(A_2 : A_2 + Angle), \end{aligned} \tag{21}$$

where $\mathbf{p}_f^i$ and $\mathbf{p}_l^i$ with $i = (L, H)$ represent the projection data under full-scan and limited-angle scan. A_1 is $0°$, A_2 is $90°$, and $Angle$ is $90°$.

B. Parameter Setting

The algorithms in the DL-based comparison experiment and ablation experiment were implemented using Python's TensorFlow framework. The computer configurations are as follows: Intel(R) Core (TM) i9-9990K 3.6GHz CPU; NVIDIA RTX 3090 GPU with 24G memory. The sub-networks IP-Net, DIP-Net, and DSP-Net of SPEAR-Net are trained simultaneously. As for the α, β, andγ in Eq.15, a progressive improvement strategy [45] was employed to adjust them. First, we set α and $\beta, \gamma = 0$ to obtain a baseline. Then β was tuned with $\alpha = 1$ and $\gamma = 0$. Finally, γ was tuned with fixed α and β until the loss function was not decreasing, and the quality of the reconstructed dual-energy CT images was optimized. Under the guidance of extensive experiments, $\alpha = 1$, $\beta = 0.1$, and $\gamma = 0.025$ were set in Eq.15. At this time, the learning rate λ was initially set to 10^{-4} and then decayed to 10^{-5}. The batch size was 1 and Adam optimizer with default settings was employed. The total training epoch was set to 100. The IP-Net and DIP-Net are trained with 9269 paired DE CT images of size 512×512. The DSP-Net was trained with 9269 paired DE projection data of size 736×576.

C. Results and analysis of comparison experiments

To validate the performance of the proposed SPEAR-Net, the FBP (filtered back projection) algorithm, CSI-GAN [46], An-Net [47], CT-Net [48] were treated as the comparisons. Besides, the mean absolute error (MAE), peak single-to-noise ratio (PSNR), and structural similarity index (SSIM) were adopted to evaluate the performance of various reconstruction methods. Four axial reconstruction results and the corresponding regions-of-interest (ROIs) of various algorithms are illustrated in Fig.3. It can be seen that FBP induces serious streak artifacts and loses diagnostic information in Fig.3(b1)-(b4). These expose the limitation of traditional reconstruction algorithms for limited-angle DECT. By deeply exploiting the essential characteristics of DECT images, DL-based methods comprehensively outperform traditional algorithms. Assisted by inpainting sinogram data using real sinogram data, the CSI-GAN algorithm gains better visual quality than FBP in artifact removal and tissue restoration. However, compared with other deep learning-based methods, CSI-GAN still fails to reconstruct satisfactory images. Compared with the single projection domain processing method, the three dual-domain deep learning-based processing methods, AN-Net, CT-Net, and SPEAR-Net, can better eliminate noise and remove artifacts in Fig.3(d1)-(f4). Specifically, CT-Net and SPEAR-Net, which have dual-flow, dual-domain characteristics, are better at preserving organ detail and better-facilitating tissue recovery than An-Net, but SPEAR-Net is the highest performer of the three(as specifically indicated by yellow arrows in red rectangular in Fig.3(d1)-(f1)(d4-f4)). The sagittal and coronal results of different reconstruction algorithms are presented in Fig.4, and the magnified ROIs in red rectangles are placed left in the corresponding images. We can observe that the FBP reconstructed images are severely degraded by noise and artifacts. The pre-processing technology, CSI-GAN, almost cannot restore the subtle features, especially in red rectangular in Fig.4(c1). Images reconstructed by An-Net suffer from the over-smooth, especially in red rectangular in Fig.4(d1). With the introduction of redundant information in the energy and spatial domains, CT-Net eliminates the over-smooth, but the reconstructed image is blurring(Fig.4(e1)). Compared with CSI-GAN, An-Net, and CT-Net, SPEAR-Net can preserve the subtle features better, as pointed out by yellow arrows in Fig.4(f2). SPEAR-Net demonstrates promising performance in structural fidelity after fully utilizing prior knowledge of the projection and image domains.

Quantitative analysis was also conducted to evaluate the proposed SPEAR-Net. Three metrics, MAE, SSIM, and PSNR, were calculated for all the test slices. The average scores of all slices are listed in TableI and the best scores are in bold. TableI shows that the FBP algorithm leads to the worst assessments in all cases. These results claim that traditional algorithms fail to reconstruct high-quality images when the projection data are incomplete. Meanwhile, it is observed that all the DL-based methods obtain superior performance compared to FBP

This article has been accepted for publication in IEEE Transactions on Instrumentation and Measurement. This is the author's version which has not been fully edited and content may change prior to final publication. Citation information: DOI 10.1109/TIM.2023.3260280

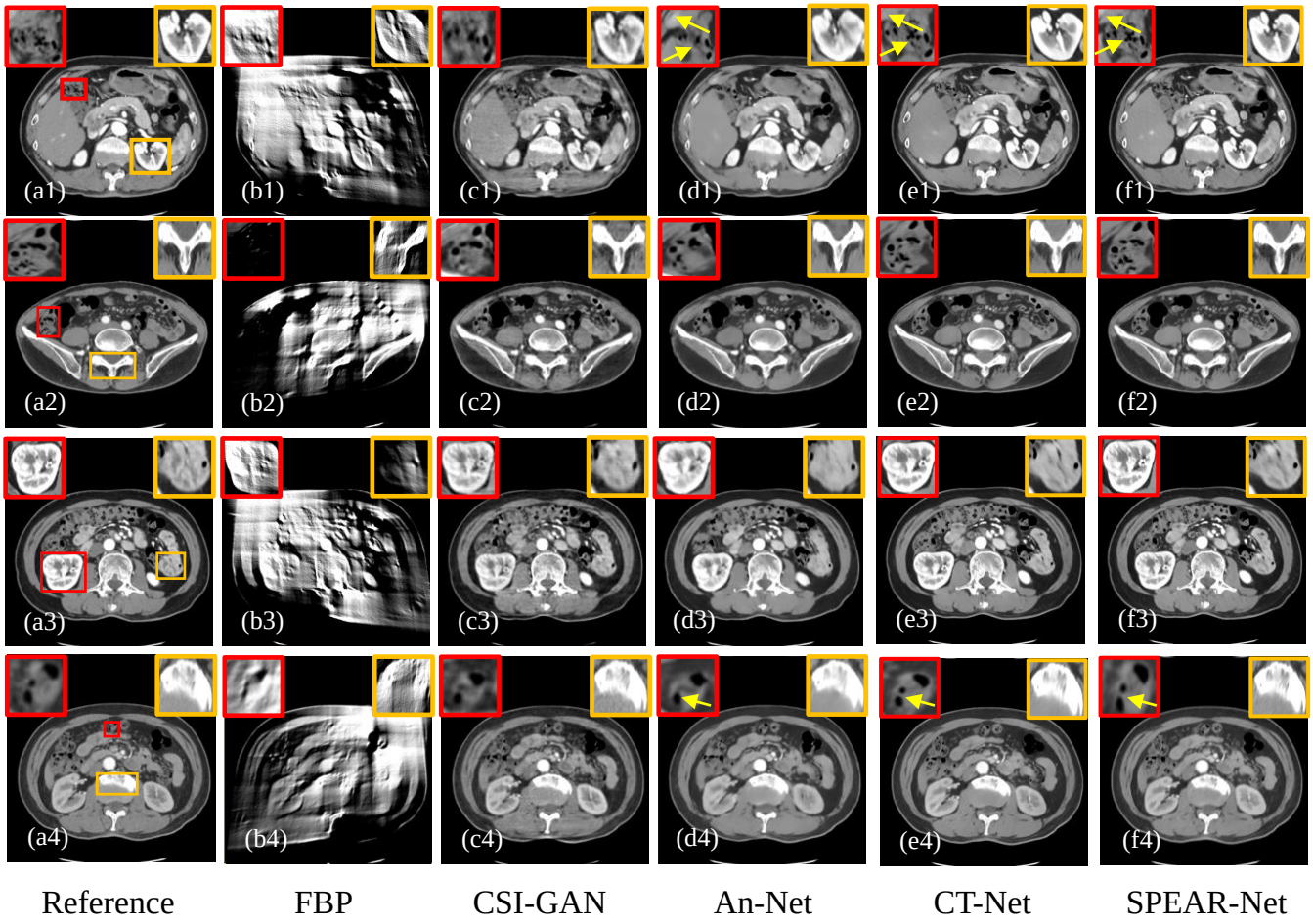

Fig. 3. The axial results of case1 with different reconstruction methods in comparison experiments. The display window is [-140, 260] HU.

TABLE I
QUANTITATIVE RESULTS FOR DIFFERENT RECONSTRUCTION METHODS IN THE COMPARISON EXPERIMENT. THESE METRICS WERE CALCULATED FOR ALL SLICES OF THE TEST SET AND THE AVERAGE SCORES FOR ALL SLICES ARE LISTED IN THE TABLE

Patients	Metrics	FBP	CSI-GAN	AN-Net	CT-Net	SPEAR-Net
Case1	MAE	357.9843	21.5024	16.314	13.7162	**9.0273**
	SSIM	52.5024	94.6923	97.6036	98.0168	**99.1309**
	PSNR	9.8341	35.4214	38.3896	39.4347	**43.9295**
Case2	MAE	357.7236	21.4867	16.7408	16.3021	**10.6613**
	SSIM	52.7607	95.1582	96.3563	98.0839	**98.3693**
	PSNR	9.9875	35.9739	38.1434	38.9834	**42.8852**
Case3	MAE	350.4455	21.0506	15.9712	16.4002	**10.0553**
	SSIM	53.122	95.8099	95.7556	97.0162	**98.9455**
	PSNR	9.8893	36.6345	37.7836	39.4047	**43.0215**

TABLE II
THE STATISTICAL PROPERTIES(MEAN ± STANDARD DEVIATION) OF DIFFERENT ALGORITHMS IN THE COMPARISON EXPERIMENT

Materials	ROI	Reference	FBP	CSI-GAN	An-Net	CT-Net	SPEAR-Net
VNC Image(HU)	ROI I	20.134±42.026	228.792±507.273	51.473±**34.624**	48.968±22.887	42.734± 21.397	**22.158**±34.43
	ROI II	3.698±103.094	-50.899±341.115	39.972±92.131	14.505±100.072	16.931±97.119	**8.8324±103.083**
	ROI III	22.026±41.793	-15.697±351.123	43.676±45.7	39.496±32.089	45.115±29.934	**27.728±42.49**
Iodine Map(%)	ROI IV	0.891±0.846	0.105±1.496	0.682±0.693	0.741±0.754	0.796±0.808	**0.844±0.825**
	ROI V	0.461±0.46	1.174±1.356	0.336±0.368	0.4±0.368	0.42±0.39	**0.454±0.447**
	ROI VI	0.966±0.855	0.298.±2.281	0.769±0.531	0.885±0.741	0.845±0.747	**0.977±0.836**

algorithms in all imaging conditions. Notably, the proposed SPEAR-Net gains the best metric results with at least 4.69 HU decrements in MAE, 3.62 dB improvement in PNSR, and 0.29 promotion in SSIM compared to other advanced DL-based methods.

VNC images and iodine maps derived from limited-angle

This article has been accepted for publication in IEEE Transactions on Instrumentation and Measurement. This is the author's version which has not been fully edited and content may change prior to final publication. Citation information: DOI 10.1109/TIM.2023.3260280

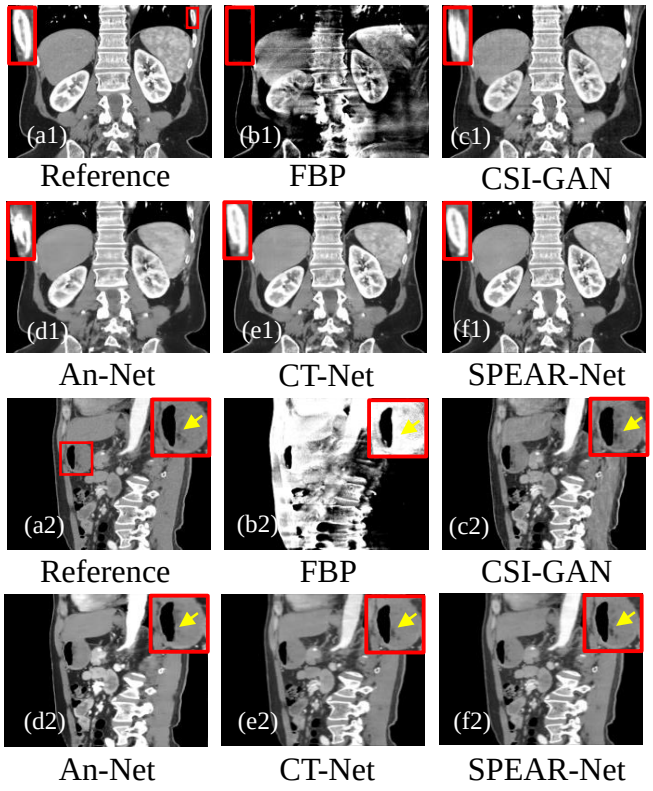

Fig. 4. The sagittal and coronal results of different reconstruction algorithms in comparison experiments. (a1)-(f1) and (a2)-f(2) are the reconstruction results of case2 and case3, respectively. The display window is [-140, 260] HU.

DECT images processed by different methods in comparison experiments are shown in Fig.5. As can be seen from Fig.5(b1)-(b6), the corresponding VNC images and iodine maps are seriously degraded due to the FBP reconstructed DECT images suffering from severe artifacts and noise. It can be seen that all deep learning-based techniques except CSI-GAN derive VNC images and iodine maps that successfully suppress most of the artifacts and recover most of the tissue features in all cases. From Fig.5(c1)-(c6), it can be seen that the VNC images and iodine maps derived from the dual-energy CT images reconstructed by the CSI-GAN method, which is filled with a large number of streaking artifacts, still have a large number of artifacts. This phenomenon illustrates the insufficiency of processing dual-energy limited-angle data in the sinogram domain alone. It is observed that the VNC images derived from dual-energy CT images reconstructed by AN-Net and CT-Net with reconstruction methods working in both projection and image domains, are over-smooth and fail to recover tissue details, as indicated by yellow arrows in Fig.5(d3)-(e3). Iodine maps generated from the CT image reconstructed by SPEAR-Net are closest to the one generated from the reference image, as indicated by the red arrows in Fig.5(d4)-(f4). The statistical properties(mean ± standard deviation) are performed on six representative ROIs selected from the VNC images and iodine maps to evaluate the quantification accuracy, and the results are listed in TableII. From TableII, it can be observed that SPEAR-Net is the best in preserving quantitative accuracy in VNC images and iodine maps. The quantitative analysis metrics (mean) of ROI I in the derived iodine maps for the SPEAR-Net reconstructed DECT image are not the best, but its standard deviation metric is the closest to that of the reference image. To sum up, SPEAR-Net not only eliminates noise and removes artifacts, but also preserves quantitative accuracy, which demonstrates the greater potential of SPEAR-Net reconstructed images for clinical applications.

D. Results and analysis of ablation experiments

An ablation study was performed to probe the effectiveness of mask operation, IP-Net, DSP-Net, and DIP-Net in the proposed SPEAR-Net. As for the ablation analysis, a progressive verification strategy was adopted. A one-step dual-energy limited-angle reconstruction network CT-Net working simultaneously in the high- and low-energy domains in the projection and image domains is considered the baseline model. First, the same masking operation as SPEAR-Net was introduced by CT-Net, which is termed as CM-Net. Then, IP-Net, which can extract prior information of a dual-energy CT image under alternating high- and low-energy dual quarter-scan (half-scan), is then incorporated into the CM-Net. Next, DIP-Net which can extract prior information from two CT images at high and low energy quarter scans, respectively, is added to the model again. Finally, DSP-Net, which can combine the prior knowledge extracted from IP-Net and DIP-Net respectively with the original dual-energy limited-angle projection data for feature fusion and data complementation, is added to the model.

Four axial slices are illustrated in Fig.6. It can be seen that each method in the ablation experiment improved the reconstruction quality and removed artifacts. The blood vessels (pointed by red arrows) cannot be well identified in the reconstructed results using CT-Net, as presented in Fig.6(b1). Fig.6(c1)-(f1) all recover the vessel details well and the reconstructed images can better close to the reference image. This indicates that the mask operation has a positive contribution to dual-energy limited-angle projection data complementation and feature fusion. Due to the contribution of prior feature information from the image under the half-scan caused by the alternating high- and low-energy scans, (d1)-(d4) in Fig.6 performs better than (c1)-(c2) in terms of structure recovery, but the reconstructed image with IP-Net incorporated on the base of CM-Net is overly smooth compared with (e1)-(e4), which is possibly limited by the repeated use of convolutions in DIP-Net and IP-Net. The DSP-Net was introduced to fuse the features of a projection equal to the prior CT image at half-scan and two projections of the CT image at quarter-scan with high and low energy respectively for data complementation. This allows SPEAR-Net to introduce self-prior information in both the projection and image domains simultaneously, which can better capture global features and can generate more uniform images(as observed in (f1)-(f4) in Fig.6). In addition, the proposed SPEAR-Net achieves the best performance in edge preservation (as pointed out by the red arrow in Fig.6(a3)-(f3)).

The sagittal and coronal results of different reconstruction algorithms in ablation experiments are presented in Fig.7.

This article has been accepted for publication in IEEE Transactions on Instrumentation and Measurement. This is the author's version which has not been fully edited and content may change prior to final publication. Citation information: DOI 10.1109/TIM.2023.3260280

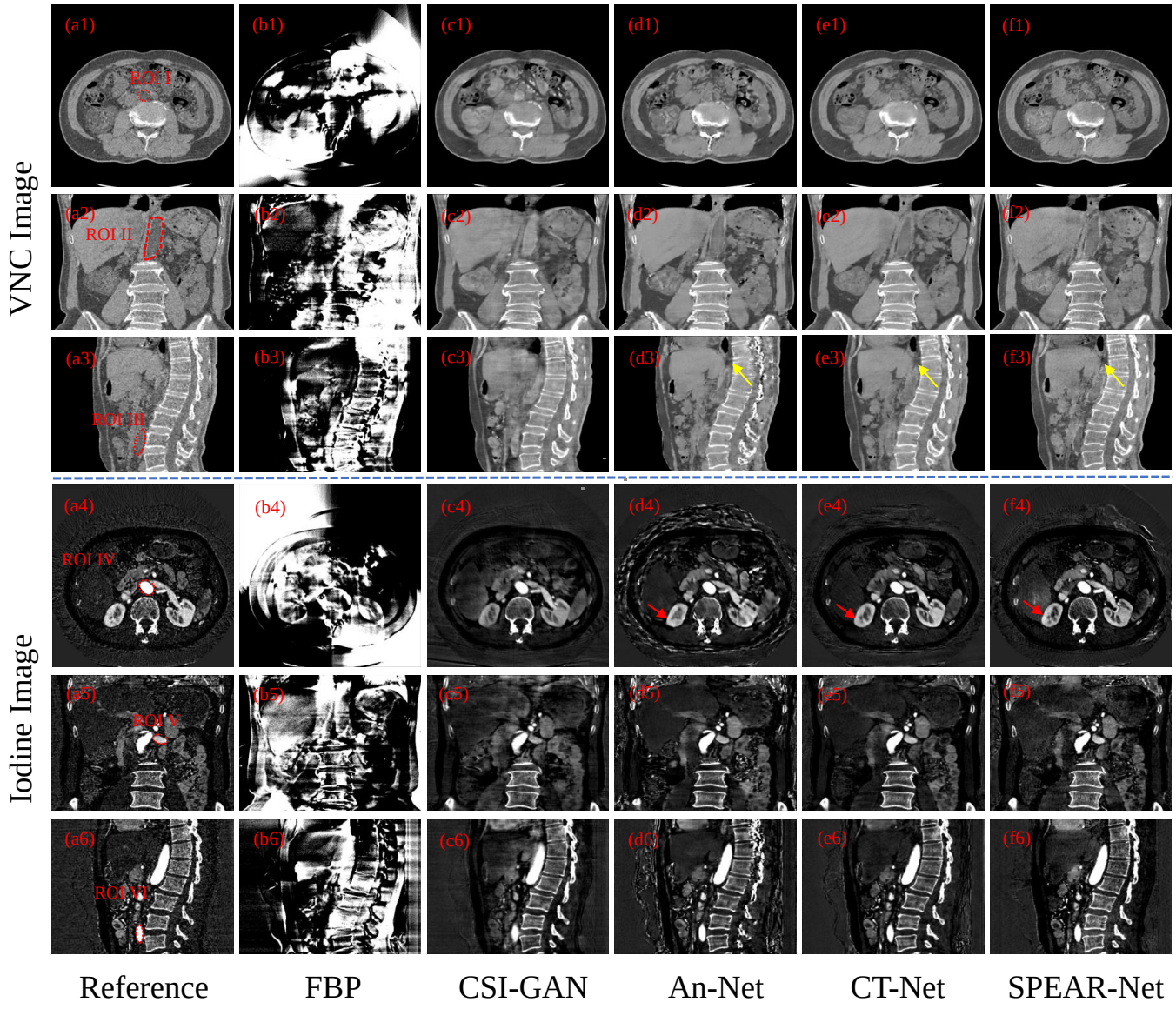

Fig. 5. VNC images and iodine maps of different methods in comparison experiments. (a1)-(f1) and (a4)-(f4) are VNC images and iodine maps of case1, (a2)-(f2) and (a5)-(f5) are VNC images and iodine maps of case2, with (a3)-(f3) and (a6)-(f6) are VNC images and iodine maps of case3. The VNC images are displayed in [-160, 240] HU, and the iodine maps are displayed in [0.5, 1.4] HU.

TABLE III

QUANTITATIVE RESULTS FOR DIFFERENT RECONSTRUCTION METHODS IN THE ABLATION EXPERIMENT. THESE METRICS WERE CALCULATED FOR ALL SLICES OF THE TEST SET AND THE AVERAGE SCORES FOR ALL SLICES ARE LISTED IN THE TABLE

Patients	CT-Net	Mask operation	IP-Net	DIP-Net	DSP-Net	MAE(HU)	SSIM(%)	PSNR(dB)
Case1	✓					13.7162	98.0168	39.4737
	✓	✓				10.8252	98.9526	42.1458
	✓	✓	✓			10.8582	99.0422	42.4371
	✓	✓	✓	✓		9.0311	99.1094	42.6400
	✓	✓	✓	✓	✓	**9.0273**	**99.1309**	**44.9295**
Case2	✓					13.5534	98.2365	40.3239
	✓	✓				12.1120	98.5327	41.0504
	✓	✓	✓			12.6726	98.6214	41.3328
	✓	✓	✓	✓		10.6613	98.7373	41.6206
	✓	✓	✓	✓	✓	**10.5769**	**99.9693**	**42.8852**
Case3	✓					12.5326	98.2463	40.3652
	✓	✓				12.2642	98.5521	40.7649
	✓	✓	✓			11.1705	98.7951	41.9335
	✓	✓	✓	✓		10.1945	98.9269	42.8008
	✓	✓	✓	✓	✓	**10.0553**	**98.9455**	**43.0215**

This article has been accepted for publication in IEEE Transactions on Instrumentation and Measurement. This is the author's version which has not been fully edited and content may change prior to final publication. Citation information: DOI 10.1109/TIM.2023.3260280

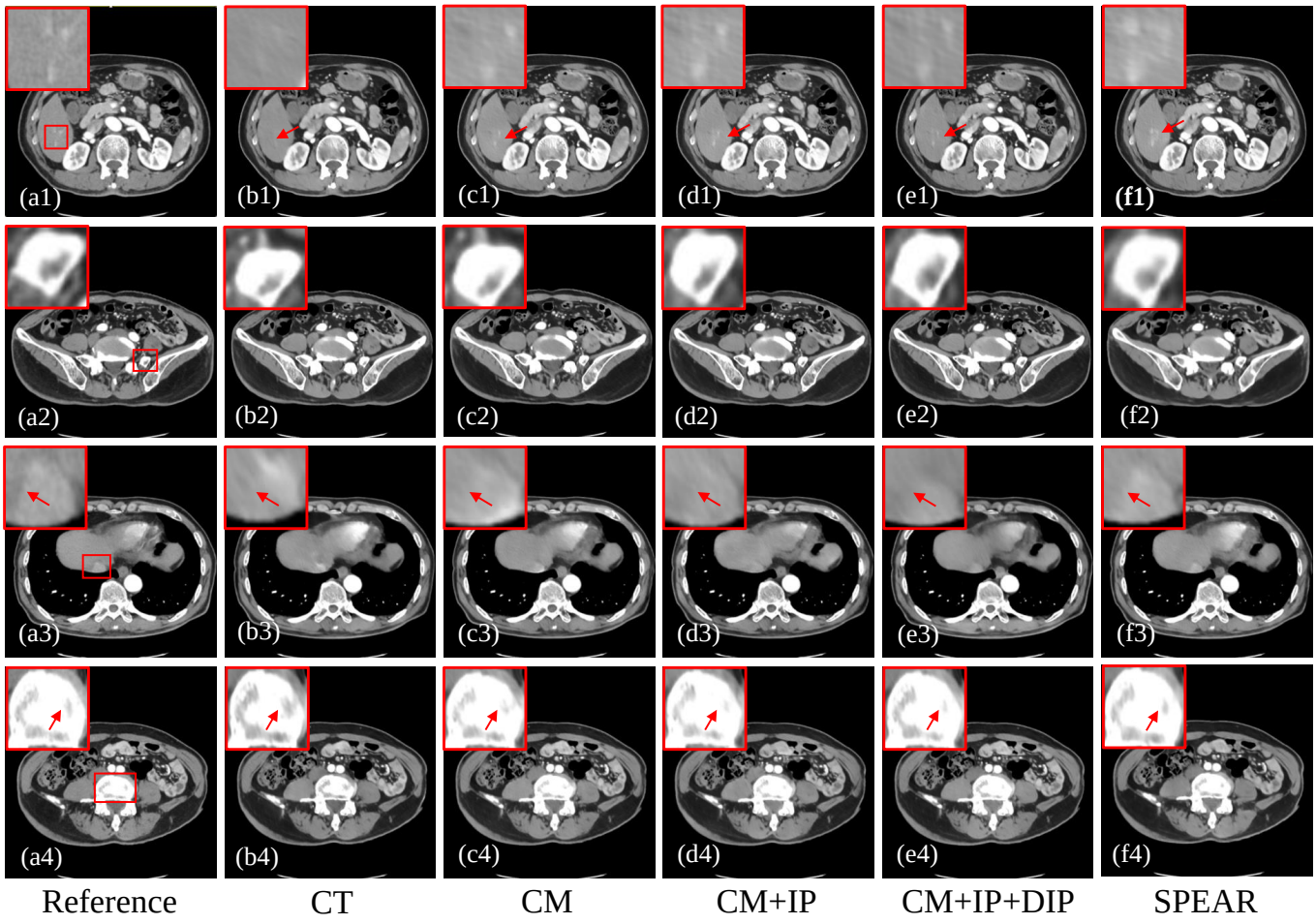

Fig. 6. The axial results of case1 with different reconstruction methods in ablation experiments. The display window is [-140, 260] HU.

As can be observed in Fig.7, the reconstruction methods by CT-Net and CM-Net produced some bar artifacts(as pointed out by the yellow arrow in Fig.7(b1)-(c1)). By exploring and exploiting the anatomical consistency, energy-domain redundancy, and comprehensive domain prior knowledge, the proposed SPEAR-Net restore reliable anatomical information and achieves promising performance in subtle structure restoration as pointed by the red arrows in (b2)-(f2) in Fig.7.

TableIII provides the quantitative evaluations for the progressive ablation study. It can be noticed that the mask operation produces better assessment scores compared to the baseline since the mask operation incorporates part of the full-scan projection in the dual-energy limited-angle projection, which makes the projection data more feature-rich. Besides, based on the IP-Net, the DIP-Net can mine more rich self-prior information in image domains in the high- and low-energy domains and brings improvements in MAE, PSNR, and SSIM. It is worth noting that SPEAR-Net obtains the best performance in all comparisons, validating the effectiveness of exploiting self-prior knowledge in the projection domain. VNC images and iodine maps derived from limited-angle DECT images processed by different methods in ablation experiments are shown in Fig.8. It can be observed from Fig.8 that the VNC images and iodine maps derived from the reconstructed images processed by all methods in the ablation experiment are effective in eliminating noise and removing artifacts. However, the VNC images generated from the CT-Net reconstructed images produced some bar artifacts(as indicated by the yellow arrow in Fig.8(b2)). SPEAR-Net was able to generate more detailed textures of the tissue closest to the reference image than each method in the ablation experiment(as indicated by the yellow circle in Fig.8(a6)-(f6)). With the incorporation of IP-Net and DIP-Net, the VNC derived from each reconstruction method is getting closer to the VNC image derived from the reference image, and the tissue edges may become blurred due to the increase of convolution operations, but SPEAR-Net can make up for this shortcoming well by using the self-prior knowledge learned from the projection domain(as indicated by the yellow arrow in Fig.8(a1)-(f1)). We performed statistics (mean ± standard deviation) on six representative ROIs selected from the VNC images and iodine maps derived from each method in the ablation experiment to assess the accuracy of quantification, and the results are listed in Table.IV. From Table.IV, it can be observed that the mean of both the VNC and the ROI of the iodine maps derived from the SPEAR-Net reconstructed images are the closest to the reference image. In ROI VI, SPEAR-Net performs worse than CM-Net in quantification accuracy preservation (smaller standard deviations), and it

This article has been accepted for publication in IEEE Transactions on Instrumentation and Measurement. This is the author's version which has not been fully edited and content may change prior to final publication. Citation information: DOI 10.1109/TIM.2023.3260280

TABLE IV
THE STATISTICAL PROPERTIES(MEAN ± STANDARD DEVIATION) OF DIFFERENT ALGORITHMS IN THE ABLATION EXPERIMENT

Materials	ROI	Reference	CT	CM	CM+IP	CM+IP+DIP	SPEAR-Net
VNC Image(HU)	ROI I	15.261±40.104	19.831±30.286	17.207±30.963	22.814±31.575	31.137±28.618	**16.982±33.582**
	ROI II	9.95±40.84	27.218±31.517	24.183±32.553	32.064±35.379	29.656±32.998	**8.681±32.998**
	ROI III	10.479±34.544	23.53±29.129	23.63±29.121	34.228±32.312	31.135±31.994	**10.508±34.525**
Iodine Map(%)	ROI IV	1.311±0.725	1.287±0.714	1.27±0.711	1.255±0.749	1.281±0.752	**1.314±0.727**
	ROI V	0.118±0.282	0.098±0.233	0.137±0.255	0.125±0.267	0.155±0.254	**0.12±0.272**
	ROI VI	0.577±0.468	0.627±0.447	0.601±**0.469**	0.515±0.424	0.597±0.434	**0.567**±0.444

TABLE V
CALCULATION COST OF DIFFERENT METHODS (UNIT: SECOND)

Method	FBP	CSI-GAN+SART-TV	AN-Net	CT-Net	SPEAR-Net
Time	27.27	29000.65	94.23	93.91	96.06

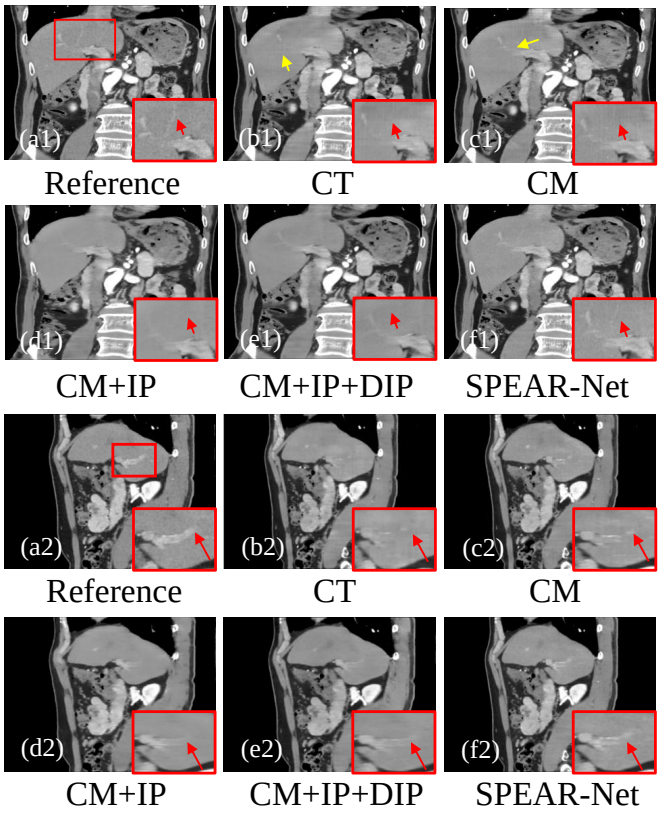

Fig. 7. The sagittal and coronal results of different reconstruction methods in ablation experiments. (a1)-(f1) and (a2)-f(2) are the reconstruction results of case2 and case3, respectively. The display window is [-140, 260] HU.

demonstrates a little worse performance in noise suppression. Overall, the more accurate SPEAR-Net-generated VNC imaging with preserved quantitative accuracy can simulate a scan without a contrast agent, better alleviating the need for no-contrast-agent scanning during clinical contrast-enhanced dual-energy imaging. More accurate measurement of iodine quantification generated by SPEAR-Net is of great clinical significance for subjectively assessing the various lesions.

E. Computational Cost

Table.V presents the computational cost of different methods with 1022 slices for 3 patients. CSI-GAN is a GAN-based projection data complementation method, and the complemented projection data are transformed to the image domain using the SART-TV method. The SART-TV reconstruction method requires interative calculations and takes a longer time compared with other methods. In contrast to CT-Net and AN-Net, SPEAR-Net introduces self-prior information in both the projection and image domains, which takes longer time than CT-Net and AN-Net. This is the reason why CT images reconstructed by SPEAR-Net are of higher quality than those reconstructed by CT-Net and AN-Net. This phenomenon is acceptable.

IV. DISCUSSION AND CONCLUSION

Recently, numerous methods [39], [40], [46], [48]–[50] have been developed to deal with the problem that limited-angle reconstruction is incomplete for projection data, and they have achieved remarkable achievement in limited-angle reconstruction. However, none of these methods explore and exploit the dual-energy limited-angle image information and projections as prior knowledge to improve imaging quality. Our developed SPEAR-Net can effectively fuse the prior information of dual-energy CT images and projections with the redundant information in the energy and spatial domains, allowing a one-step reconstruction of high-quality dual-energy limited-angle images, reducing the radiation dose and shortening scan time. First, SPEAR-Net introduces the mask operation, which positively contributes to the feature fusion between dual-energy limited-angle projection and dual-energy full-scan projection. Then, the addition of IP-Net after the mask operation facilitates the extraction of prior information from dual-energy CT images with alternating high- and low-energy dual-quarter-scan. Next, DIP-Net, which can extract prior information from two CT images under high-energy and low-energy quarter scans, respectively, is again empowered into the model. Finally, DSP-Net, which can combine prior knowledge extracted from IP-Net and DIP-Net, respectively, with the original dual-energy limited-angle projection data, is enhanced by the introduction of SPEAR-Net for feature fusion and data complementation. Both qualitative and quantitative reconstruction results show that SPEAR-Net has remarkable performance in artifact removal, noise elimination, and tissue structure preservation. The excellent performance of SPEAR-

This article has been accepted for publication in IEEE Transactions on Instrumentation and Measurement. This is the author's version which has not been fully edited and content may change prior to final publication. Citation information: DOI 10.1109/TIM.2023.3260280

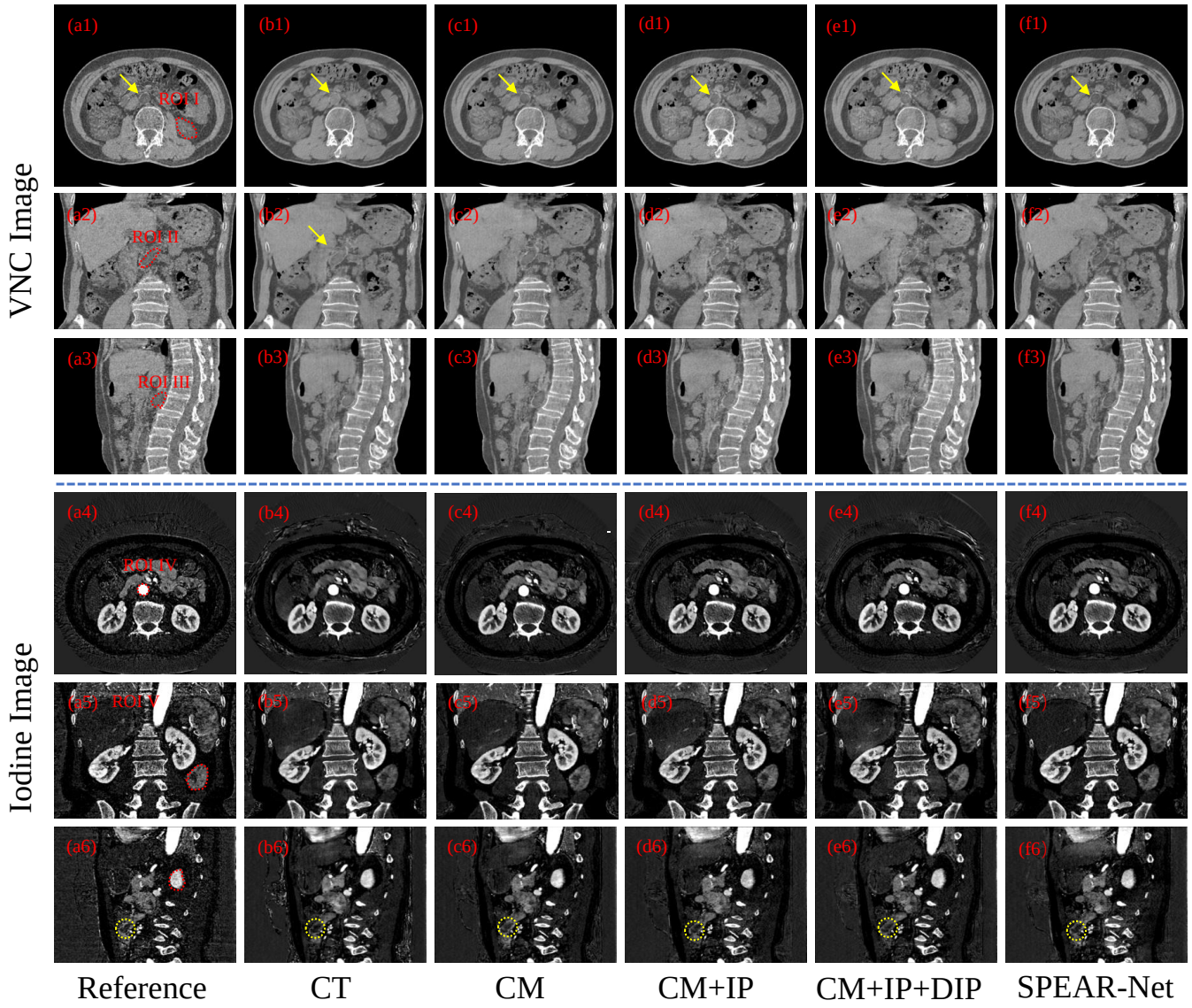

Fig. 8. VNC images and iodine maps of different methods in ablation experiments. (a1)-(f1) and (a4)-(f4) are VNC images and iodine maps of case1, (a2)-(f2) and (a5)-(f5) are VNC images and iodine maps of case2, with (a3)-(f3) and (a6)-(f6) are VNC images and iodine maps of case3. The VNC images are displayed in [-160, 240] HU, and the iodine maps are displayed in [0.5, 1.4] HU.

Net-derived virtual non-contrast (VNC) imaging and iodine contrast quantification demonstrates that SPEAR-Net simulates scans without contrast and can better alleviate the need for contrast-free scans in clinical contrast-enhanced dual-energy imaging

Although the SPEAR-Net demonstrates encouraging improvement in dual-energy limited-angle CT reconstruction, some issues are still to be noticed. Limited by current technical bottlenecks, there may be noise and artifacts left in the ground truth images, which may lower the performance of the proposed algorithm in sagittal and coronal reconstruction results. There is room for improvement in the extraction and utilization of prior information for dual-energy limited-angle images and projections because the high- and low-frequency prior information components are not better empowered by the distinction in the global space. Therefore, how to reconstruct the energy and spatial domains with more frequency-level prior feature space is still an open issue. The network performance of SPEAR-Net does not overcome the drawback of relying on the integrity of the projected data, i.e., the small range of scanning angles, which improves little relative to other algorithms. The effective integration of deep learning into traditional iterative strategies remains a challenge. When extracting prior information from CT images, the image edges are blurred and the reconstructed images are over-smooth due to the extensive use of convolution operations, which leads to performance degradation. Therefore, how to balance the over-smoothing and effective artifact removal in SPAER-Net is a problem that needs attention in the future. The data simulation in this paper was carried out through a simple Radon transform without considering the polychromatic x-ray interaction or complex detector responses. This is because we want to test the

This article has been accepted for publication in IEEE Transactions on Instrumentation and Measurement. This is the author's version which has not been fully edited and content may change prior to final publication. Citation information: DOI 10.1109/TIM.2023.3260280

feasibility of the proposed SPEAR-Net in retrieving dual energy information from limited angle measurement by avoiding other confounding factors. Investigation of the performance of the proposed method on real experimental data or simulated data involving more realistic x-ray interactions can be future work.

V. ACKNOWLEDGMENT

The authors would like to thank the Nanjing General PLA Hospital for providing clinical data, and data are adherent to the tenets of the Declaration of Helsinki.

REFERENCES

[1] Z. Huang, J. Zhang, Y. Zhang, and H. Shan, "DU-GAN: Generative Adversarial Networks with dual-domain U-net-based discriminators for low-dose CT denoising," *IEEE Transactions on Instrumentation and Measurement*, vol. 71, pp. 1–12, 2021.

[2] P. Chen, Y. Han, and Y. Li, "X-ray multispectrum CT imaging by projection sequences blind separation based on basis-effect decomposition," *IEEE Transactions on Instrumentation and Measurement*, vol. 70, pp. 1–8, 2020.

[3] D. Kalasová *et al.*, "Wide-cone angle phase-contrast X-ray computed tomography of synthetic polymer materials," *IEEE Transactions on Instrumentation and Measurement*, vol. 69, no. 11, pp. 8910–8918, 2020.

[4] X. Li, S. Wang, P. Chen, and L. Wang, "3-D inspection method for industrial product assembly based on single X-ray projections," *IEEE Transactions on Instrumentation and Measurement*, vol. 70, pp. 1–14, 2021.

[5] G. Wang, H. Yu, and B. De Man, "An outlook on X-ray CT research and development," *Medical physics*, vol. 35, no. 3, pp. 1051–1064, 2008.

[6] D. Yamak, P. Panse, W. Pavlicek, T. Boltz, and M. Akay, "Non-calcified coronary atherosclerotic plaque characterization by dual energy computed tomography," *IEEE journal of biomedical and health informatics*, vol. 18, no. 3, pp. 939–945, 2013.

[7] A. C. Silva, B. G. Morse, A. K. Hara, R. G. Paden, N. Hongo, and W. Pavlicek, "Dual-energy (spectral) CT: applications in abdominal imaging," *Radiographics*, vol. 31, no. 4, pp. 1031–1046, 2011.

[8] M.-J. Kang, C. M. Park, C.-H. Lee, J. M. Goo, and H. J. Lee, "Dual-energy CT: clinical applications in various pulmonary diseases," *Radiographics*, vol. 30, no. 3, pp. 685–698, 2010.

[9] S. Wang, H. Yu, Y. Xi, C. Gong, W. Wu, and F. Liu, "Spectral-image decomposition with energy-fusion sensing for spectral CT reconstruction," *IEEE Transactions on Instrumentation and Measurement*, vol. 70, pp. 1–11, 2021.

[10] W. Wu, D. Hu, K. An, S. Wang, and F. Luo, "A high-quality photon-counting CT technique based on weight adaptive total-variation and image-spectral tensor factorization for small animals imaging," *IEEE Transactions on Instrumentation and Measurement*, vol. 70, pp. 1–14, 2020.

[11] M. Cho, H. Kim, H. Youn, and S. Kim, "A feasibility study of digital tomosynthesis for volumetric dental imaging," *Journal of Instrumentation*, vol. 7, no. 03, p. P03007, 2012.

[12] A. Tingberg, "X-ray tomosynthesis: a review of its use for breast and chest imaging," *Radiation protection dosimetry*, vol. 139, no. 1-3, pp. 100–107, 2010.

[13] Z. Wang *et al.*, "Low-dose multiple-information retrieval algorithm for X-ray grating-based imaging," *Nuclear Instruments and Methods in Physics Research Section A: Accelerators, Spectrometers, Detectors and Associated Equipment*, vol. 635, no. 1, pp. 103–107, 2011.

[14] L. Li, Z. Chen, L. Zhang, and K. Kang, "An exact reconstruction algorithm in variable pitch helical cone-beam CT when PI-line exists," *Journal of X-ray Science and Technology*, vol. 14, no. 2, pp. 109–118, 2006.

[15] X. Duan, L. Zhang, Y. Xiao, J. Cheng, Z. Chen, and Y. Xing, "Metal artifact reduction in CT images by sinogram TV inpainting," in *2008 IEEE Nuclear Science Symposium Conference Record*. IEEE, 2008, pp. 4175–4177.

[16] Y. Li *et al.*, "Strategy of computed tomography sinogram inpainting based on sinusoid-like curve decomposition and eigenvector-guided interpolation," *JOSA A*, vol. 29, no. 1, pp. 153–163, 2012.

[17] M. Kalke and S. Siltanen, "Sinogram interpolation method for sparse-angle tomography," *Applied Mathematics*, vol. 2014, 2014.

[18] M. Benning, C. Brune, M. J. Lagerwerf, and C.-B. Schönlieb, "TGV sinogram inpainting for limited angle tomography," *Proceedings of the Royal Society A*, 2015.

[19] J. K. Choi, B. Dong, and X. Zhang, "Limited tomography reconstruction via tight frame and simultaneous sinogram extrapolation," *Journal of Computational Mathematics*, pp. 575–589, 2016.

[20] G.-H. Chen, J. Tang, and S. Leng, "Prior image constrained compressed sensing (PICCS): a method to accurately reconstruct dynamic CT images from highly undersampled projection data sets," *Medical physics*, vol. 35, no. 2, pp. 660–663, 2008.

[21] Y. Lu, J. Zhao, and G. Wang, "Few-view image reconstruction with dual dictionaries," *Physics in Medicine & Biology*, vol. 57, no. 1, p. 173, 2011.

[22] C. Schorr and M. Maisl, "Exploitation of geometric a priori knowledge for limited data reconstruction in non-destructive testing," in *Proceedings of Fully3D Conference*, 2013.

[23] D. Wu, L. Li, and L. Zhang, "Feature constrained compressed sensing CT image reconstruction from incomplete data via robust principal component analysis of the database," *Physics in Medicine & Biology*, vol. 58, no. 12, p. 4047, 2013.

[24] H. Zhang, L. Ouyang, J. Huang, J. Ma, W. Chen, and J. Wang, "Few-view cone-beam CT reconstruction with deformed prior image," *Medical physics*, vol. 41, no. 12, p. 121905, 2014.

[25] H. Dang, J. H. Siewerdsen, and J. W. Stayman, "Prospective regularization design in prior-image-based reconstruction," *Physics in Medicine & Biology*, vol. 60, no. 24, p. 9515, 2015.

[26] J. Sun *et al.*, "Automatic video analysis framework for exposure region recognition in X-ray imaging automation," *IEEE Journal of Biomedical and Health Informatics*, 2022.

[27] E. Kang, W. Chang, J. Yoo, and J. C. Ye, "Deep convolutional framelet denosing for low-dose CT via wavelet residual network," *IEEE transactions on medical imaging*, vol. 37, no. 6, pp. 1358–1369, 2018.

[28] A. Kumar, J. Kim, D. Lyndon, M. Fulham, and D. Feng, "An ensemble of fine-tuned convolutional neural networks for medical image classification," *IEEE journal of biomedical and health informatics*, vol. 21, no. 1, pp. 31–40, 2016.

[29] Z. Zhao, Z. Zeng, K. Xu, C. Chen, and C. Guan, "DSAL: Deeply Supervised Active Learning from strong and weak labelers for biomedical image segmentation," *IEEE Journal of Biomedical and Health Informatics*, vol. 25, no. 10, pp. 3744–3751, 2021.

[30] C. Sun, A. Xu, D. Liu, Z. Xiong, F. Zhao, and W. Ding, "Deep learning-based classification of liver cancer histopathology images using only global labels," *IEEE journal of biomedical and health informatics*, vol. 24, no. 6, pp. 1643–1651, 2019.

[31] L. Xie, W. Cai, and Y. Gao, "DMCGNet: A Novel Network for Medical Image Segmentation with Dense Self-mimic and Channel Grouping Mechanism," *IEEE Journal of Biomedical and Health Informatics*, vol. 26, no. 10, pp. 5013–5024, 2022.

[32] A. Lin, B. Chen, J. Xu, Z. Zhang, G. Lu, and D. Zhang, "Ds-TransUNet: Dual swin transformer u-net for medical image segmentation," *IEEE Transactions on Instrumentation and Measurement*, 2022.

[33] K. Roy, D. Banik, D. Bhattacharjee, O. Krejcar, and C. Kollmann, "LWMLA-NET: A Lightweight Multi-level Attention-Based NETwork for Segmentation of COVID-19 lungs Abnormalities From CT Images," *IEEE Transactions on Instrumentation and Measurement*, vol. 71, pp. 1–13, 2022.

[34] D. M. Pelt and K. J. Batenburg, "Fast tomographic reconstruction from limited data using artificial neural networks," *IEEE Transactions on Image Processing*, vol. 22, no. 12, pp. 5238–5251, 2013.

[35] J. Sun, H. Li, Z. Xu *et al.*, "Deep ADMM-Net for compressive sensing MRI," *Advances in neural information processing systems*, vol. 29, 2016.

[36] K. H. Jin, M. T. McCann, E. Froustey, and M. Unser, "Deep convolutional neural network for inverse problems in imaging," *IEEE Transactions on Image Processing*, vol. 26, no. 9, pp. 4509–4522, 2017.

[37] Y. Zhang *et al.*, "CD-Net: Comprehensive Domain network with spectral complementary for DECT sparse-view reconstruction," *IEEE Transactions on Computational Imaging*, vol. 7, pp. 436–447, 2021.

[38] Y. Zhang *et al.*, "CLEAR: Comprehensive Learning Enabled Adversarial Reconstruction for subtle structure enhanced low-dose CT imaging," *IEEE Transactions on Medical Imaging*, vol. 40, no. 11, pp. 3089–3101, 2021.

[39] D. Hu, Y. Zhang, J. Liu, S. Luo, and Y. Chen, "DIOR: Deep Iterative Optimization-based Residual-learning for Limited-angle CT Reconstruction," *IEEE Transactions on Medical Imaging*, 2022.

[40] D. Hu *et al.*, "SPECIAL: Single-shot Projection Error Correction Integrated Adversarial Learning for limited-angle CT," *IEEE Transactions on Computational Imaging*, vol. 7, pp. 734–746, 2021.

This article has been accepted for publication in IEEE Transactions on Instrumentation and Measurement. This is the author's version which has not been fully edited and content may change prior to final publication. Citation information: DOI 10.1109/TIM.2023.3260280

[41] H. Zhao, O. Gallo, I. Frosio, and J. Kautz, "Loss functions for image restoration with neural networks," *IEEE Transactions on computational imaging*, vol. 3, no. 1, pp. 47–57, 2016.

[42] Q. Yang *et al.*, "Low-dose CT image denoising using a generative adversarial network with wasserstein distance and perceptual loss," *IEEE transactions on medical imaging*, vol. 37, no. 6, pp. 1348–1357, 2018.

[43] J. Johnson, A. Alahi, and L. Fei-Fei, "Perceptual losses for real-time style transfer and super-resolution," in *European conference on computer vision*. Springer, 2016, pp. 694–711.

[44] S. Faby *et al.*, "Performance of today's dual energy CT and future multi energy CT in virtual non-contrast imaging and in iodine quantification: a simulation study," *Medical physics*, vol. 42, no. 7, pp. 4349–4366, 2015.

[45] D. Wu, K. Gong, K. Kim, X. Li, and Q. Li, "Consensus neural network for medical imaging denoising with only noisy training samples," in *International Conference on Medical Image Computing and Computer-Assisted Intervention*. Springer, 2019, pp. 741–749.

[46] Y. Wang *et al.*, "An effective sinogram inpainting for complementary limited-angle dual-energy computed tomography imaging using generative adversarial networks," *Journal of X-Ray Science and Technology*, vol. 29, no. 1, pp. 37–61, 2021.

[47] W. Zhang *et al.*, "Dual-energy CT Reconstruction from Dual quarter scans," *arXiv preprint arXiv:2012.11374*, 2020.

[48] K. Chen *et al.*, "CT-Net: Cascaded T-shape Network using spectral redundancy for dual-energy CT limited-angle reconstruction," *Biomedical Signal Processing and Control*, vol. 79, p. 104072, 2023.

[49] Q. Zhang, Z. Hu, C. Jiang, H. Zheng, Y. Ge, and D. Liang, "Artifact removal using a hybrid-domain convolutional neural network for limited-angle computed tomography imaging," *Physics in Medicine & Biology*, vol. 65, no. 15, p. 155010, 2020.

[50] T. Lyu *et al.*, "Estimating dual-energy CT imaging from single-energy CT data with material decomposition convolutional neural network," *Medical image analysis*, vol. 70, p. 102001, 2021.